ARTICLES
https://doi.org/10.1038/s41567-021-01327-8

nature physics

Observation of interband collective excitations in twisted bilayer graphene

Niels C. H. Hesp[1,11], Iacopo Torre[1,11], Daniel Rodan-Legrain[2,11], Pietro Novelli[3,4,11], Yuan Cao[2], Stephen Carr[5], Shiang Fang[5], Petr Stepanov[1], David Barcons-Ruiz[1], Hanan Herzig Sheinfux[1], Kenji Watanabe[6], Takashi Taniguchi[6], Dmitri K. Efetov[1], Efthimios Kaxiras[5,7], Pablo Jarillo-Herrero[2]✉, Marco Polini[4,8,9]✉ and Frank H. L. Koppens[1,10]✉

The single-particle and many-body properties of twisted bilayer graphene (TBG) can be dramatically different from those of a single graphene layer, particularly when the two layers are rotated relative to each other by a small angle ($\theta \approx 1°$), owing to the moiré potential induced by the twist. Here we probe the collective excitations of TBG with a spatial resolution of 20 nm, by applying mid-infrared near-field optical microscopy. We find a propagating plasmon mode in charge-neutral TBG for $\theta = 1.1–1.7°$, which is different from the intraband plasmon in single-layer graphene. We interpret it as an interband plasmon associated with the optical transitions between minibands originating from the moiré superlattice. The details of the plasmon dispersion are directly related to the motion of electrons in the moiré superlattice and offer an insight into the physical properties of TBG, such as band nesting between the flat band and remote band, local interlayer coupling, and losses. We find a strongly reduced interlayer coupling in the regions with AA stacking, pointing at screening due to electron–electron interactions. Optical nano-imaging of TBG allows the spatial probing of interaction effects at the nanoscale and potentially elucidates the contribution of collective excitations to many-body ground states.

When two layers of graphene are superimposed with a small twist angle θ, they form a triangular moiré lattice with a lattice constant d that is related to θ by $d = d_0/(2\sin(\theta/2))$, where $d_0 \approx 0.246$ nm is the lattice constant of single-layer graphene[1–4]. The top view of twisted bilayer graphene (TBG) reveals regions where the two sheets are locally in the AA-stacking configuration surrounded by regions where stacking is of the more energetically favoured AB-type or BA-type (Bernal stacking)[5] configuration. Electrons can tunnel from one layer to the other with an amplitude that depends on the local alignment between the two layers[1,3]. The interlayer tunnelling amplitude is, therefore, spatially modulated with the periodicity of the moiré lattice. Effectively, this produces a background scalar potential and non-Abelian gauge field, acting on the graphene Dirac fermions[6]. These two potentials (with an amplitude of the order of 100 meV) localize the electronic states close to the charge neutrality point in regions where the alignment between the two layers is an AA-like configuration[7–10]. In the band structure picture, these two contributions yield a pair of narrow bands close to the charge neutrality point at the magic angle, which—due to their high density of states—are held responsible for the observed correlated phenomena[9–19]. Switching off the scalar potential enhances the flatness of the bands, making them perfectly flat throughout the superlattice Brillouin zone at the magic angle[6,20].

Several experimental probes have been used to explore the physics of TBG, including electronic transport[9–14,21], quantum capacitance[15], scanning tunnelling microscopy[16–19] and scanning magnetometry[22], also unveiling similar phenomena in twisted double bilayer graphene[23–25] and trilayer graphene on hexagonal boron nitride (hBN) (ref. [26]). However, all these techniques are only sensitive to the static (very low frequency) response of the system. In systems where electron–electron (e–e) interactions play a dominant role, experimental techniques that probe the response to perturbations carrying a finite in-plane wavevector q and angular frequency ω are expected to be rich sources of information. One of these techniques is scattering-type scanning near-field optical microscopy (s-SNOM) (refs. [27–31]), which enables the measurement of the dispersion relation of collective electronic excitations, such as Dirac plasmons in doped graphene[27,28,32], with a spatial resolution of 20 nm. Here we apply this technique to study the optical properties of twisted graphene near the magic angle, with a particular focus on the collective excitations related to moiré minibands.

Optical properties of TBG

The order of magnitude of energy separation between the nearly flat bands and the nearest conduction and valence bands is ~100 meV for θ close to the magic angle. This justifies our interest in the optical properties and collective excitations[33–35], as probed by s-SNOM (Fig. 1a–c), in the mid-infrared region of the electromagnetic spectrum. In this region, photons have energies $\hbar\omega$ in the range of 80–200 meV, where $\hbar$ is the reduced form of Planck's constant, which is comparable to the above-mentioned energy scale. These

[1]ICFO—Institut de Ciencies Fotoniques, The Barcelona Institute of Science and Technology, Castelldefels (Barcelona), Spain. [2]Department of Physics, Massachusetts Institute of Technology, Cambridge, MA, USA. [3]NEST, Scuola Normale Superiore, Pisa, Italy. [4]Istituto Italiano di Tecnologia, Graphene Labs, Genova, Italy. [5]Department of Physics, Harvard University, Cambridge, MA, USA. [6]National Institute for Materials Science, Ibaraki, Japan. [7]Harvard John A. Paulson School of Engineering and Applied Sciences, Harvard University, Cambridge, MA, USA. [8]Dipartimento di Fisica dell'Università di Pisa, Pisa, Italy. [9]Department of Physics and Astronomy, University of Manchester, Manchester, UK. [10]ICREA—Institució Catalana de Recerca i Estudis Avançats, Barcelona, Spain. [11]These authors contributed equally: Niels C. H. Hesp, Iacopo Torre, Daniel Rodan-Legrain, Pietro Novelli. ✉e-mail: pjarillo@mit.edu; marco.polini@iit.it; frank.koppens@icfo.eu

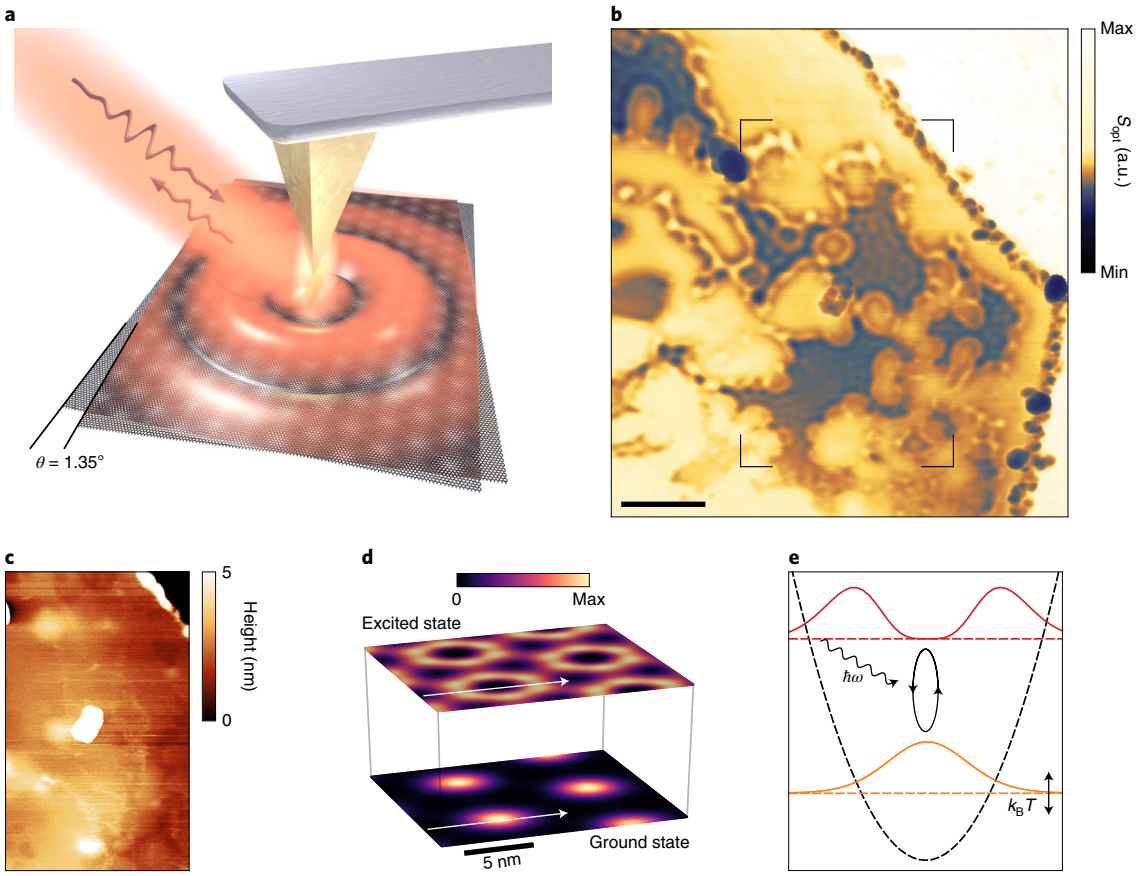

Fig. 1 | Collective excitations in TBG. a, Illustration of the s-SNOM experiment: an AFM metallic tip is illuminated by infrared light, which provides sufficient momentum to launch a collective excitation in TBG. The plasmon can, in turn (for example, by reflection from an edge or interface), scatter into light at the tip. This scattered light is detected by a photodetector. The curved arrows indicate the light impinging on the tip (coming from the laser) as well as the scattered light (going to the detector). **b**, Image of the near-field amplitude obtained by scanning the AFM tip and recording the photodetector signal. Propagating collective excitations are visible in certain areas as periodic interference fringes. The illumination photon energy is $\hbar\omega = 219$ meV and the scale bar is 500 nm. **c**, AFM image of the marked region in **b**. **d**, Square modulus of the wavefunction $|\langle \mathbf{r}|\mathbf{k}=\mathbf{K},\nu\rangle|^2$, plotted in arbitrary units, associated with one of the flat bands (bottom) and the first excited band (top), evaluated at the **K** point of the moiré superlattice Brillouin zone. These states are mostly localized around the regions with local AA stacking (which form a triangular lattice) and are involved in the relevant optical transitions. **e**, Linecuts of the wavefunctions along the white arrows in **c** represented in a harmonic confinement potential[6] (black dashed line), with the coloured horizontal dashed lines indicating the energies of the states. An interband transition occurs between the lower-energy state and excited state. A similar transition is happening, for holes, between the corresponding pair of states, approximately related to the illustrated ones by electron–hole symmetry.

energies are, on the other hand, much larger than the energy separation between the pair of nearly flat bands, considered in ref. [36].

We can qualitatively understand the optical properties of this system in the following way. When light impinges on TBG, its time-periodic electric field shakes electrons around their equilibrium positions (the AA sites, forming a triangular lattice) or—in the more rigorous language of band theory—it induces an interband transition between the ground and excited states at the **K** point of the superlattice Brillouin zone (Fig. 1d,e). If the field carries a finite in-plane wavevector q (provided by the sharp atomic force microscope (AFM) tip), the shaking electrons will build up an oscillating charge density with the same wavevector (plus harmonics due to the exchange of the reciprocal lattice vectors). This oscillating charge density, in turn, creates an oscillating electric field that adds to the external field. If q and ω are correctly matched, this induced field can be strong enough to sustain the oscillation even after the external field has been turned off. This resonant behaviour gives rise to collective modes that are called interband plasmons, which have been theoretically predicted to emerge in TBG[37,38], but were never experimentally studied so far. At $q=0$, this collective excitation has the same frequency as the bare interband transition. On increasing q, as we show in this work, it acquires a finite dispersion. Thus, these excitations do propagate with a finite group velocity, akin to graphene Dirac plasmons[27,28,39], albeit with very different dispersion. Here the dispersion depends on the degree of band nesting, which is the phenomenon of two bands being parallel in the energy–wavevector space, and details of the e–e interaction potential, which is heavily influenced by screening from nearby dielectrics. We note that a similar collective mode occurs in topological insulators[40,41] or between the rigorously flat Landau levels of a two-dimensional (2D) parabolic-band electron gas in a perpendicular magnetic field. In this case, while single electrons oscillate at the cyclotron frequency Ω_c, e–e interactions induce a collective mode, known as a bulk magnetoplasmon, which, at a long wavelength, has a linear dispersion[42] $\omega(q)=\Omega_c+sq$ with group velocity $s>0$ reflecting its propagating character. k_BT indicates the thermal energy at $T=300$ K, where k_B is the Boltzmann constant.

Near-field experiments on TBG

We now turn to a description of our experimental findings. We fabricate the TBG samples using the tear-and-stack method[43,44].

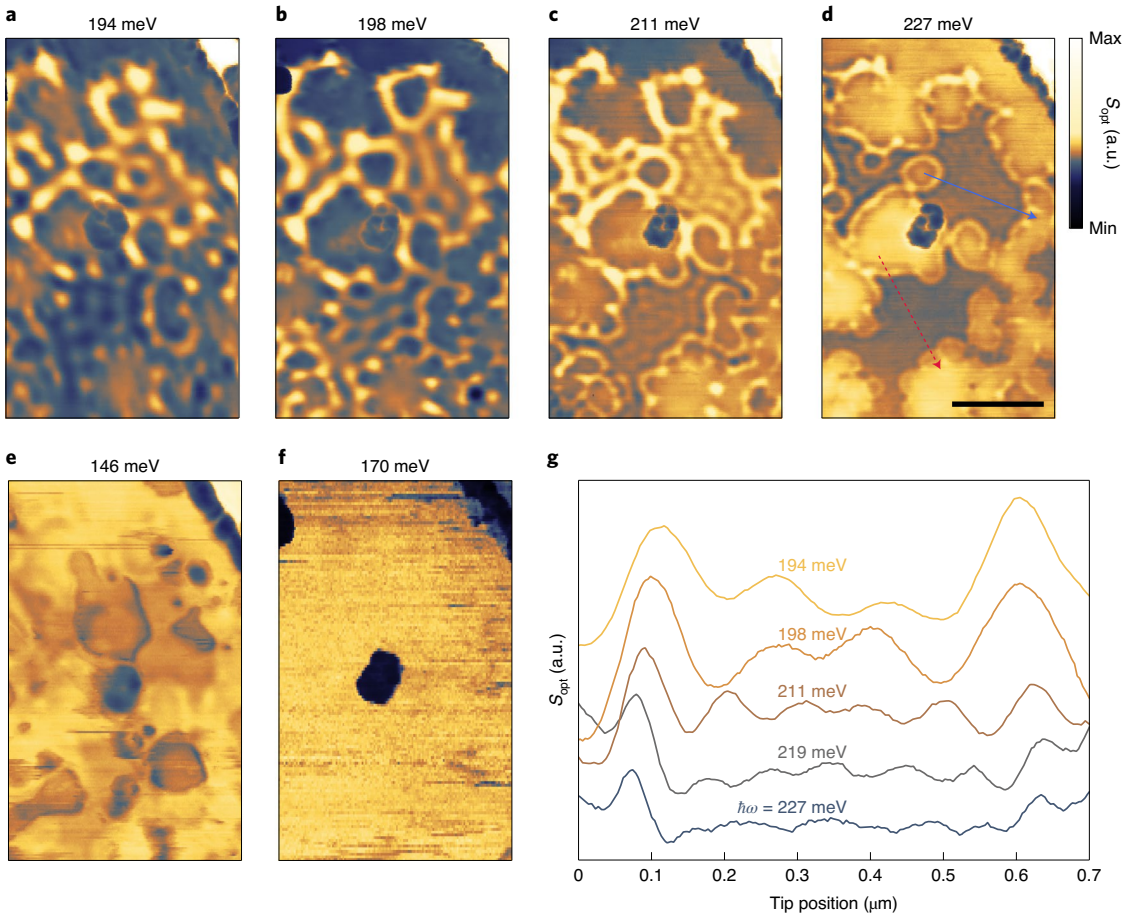

Fig. 2 | Controlling the wavelength of interband plasmons. a–f, Images of the near-field amplitude at different excitation energies $\hbar\omega$ of the area marked in Fig. 1b; $\hbar\omega > \hbar\Omega_{exp}$ (**a**–**d**), while $\hbar\omega < \hbar\Omega_{exp}$ (**e** and **f**). Solid and dashed arrows in **d** indicate the line traces associated with the data in **g** and Fig. 3a, and the scale bar is 500 nm. **g**, Line traces along the solid blue arrow in **d**, visualizing the strong dependence of plasmon wavelength on the excitation energy. Lines are vertically separated for clarity.

These are encapsulated in hBN, and placed on a metal gate (see Supplementary Note 1 for details). The twist angle θ is determined from cryogenic transport measurements[43] (Supplementary Note 2). We then perform s-SNOM measurements with mid-infrared light (free-space wavelength λ_0 in the range of 5–11 μm) in ambient conditions at $T = 300$ K. We generate a nanoscale light hotspot by focussing a laser beam on the apex of a sharp (apex radius, ~25 nm) metallic AFM tip (Fig. 1a). This hotspot interacts with the charge carriers and produces collective excitations that are reflected by interfaces, return to the tip and finally are converted into a scattered field, which is measured by a photodetector. By scanning the tip position, we simultaneously acquire a spatial map of the backscattered light intensity S_{opt} and AFM topography. Noise and far-field contributions to the optical signal are strongly reduced by locking to the third harmonic of the tapping frequency of the tip. The spatial resolution of the obtained images is limited only by the tip radius[45] (Supplementary Note 3).

Figure 1b shows a typical near-field image of TBG with no gate voltage applied (at zero applied voltage, the TBG is close to charge neutrality; Supplementary Notes 1 and 2) and an average twist angle of $\theta = 1.35°$, obtained from the transport measurements. Figure 1c shows the AFM image recorded at the same time. In the near-field image, for an excitation energy $\hbar\omega = 219$ meV, two types or region can be distinguished. Regions with a rather spatially constant response S_{opt} (yellow) and regions where S_{opt} shows clear, spatially varying and periodic features. This contrasts with a near-field map taken at a lower energy of $\hbar\omega = 146$ meV, in which the periodic features are absent (Fig. 2e). As reported, scanning superconducting quantum interference device measurements on similar samples have shown[22] that some regions can exhibit magic-angle behaviour while some other regions do not (for example, due to lattice relaxation into an angle far from the magic angle). In this work, we focus on the regions with varying and periodic features of this device. Supplementary Notes 1 and 4 provide results from 14 other devices with $\theta = 1.1–1.7°$ and a discussion on the correlation of these regions with tiny topographic features.

In the regions of interest, S_{opt} displays an oscillatory spatial behaviour. The latter has a characteristic period of ~80 nm in all of the regions of interest (with a ±10 nm spread), about one order of magnitude larger than d. We attribute this oscillatory behaviour to the excitation of a propagating collective electronic mode. The fact that we observe these interference patterns in ungated TBG is in stark contrast with the intraband collective electronic excitations (Dirac plasmons) of single-layer and bilayer graphene, where high doping levels (above 10^{13} cm^{-2}) are required to propagate at the frequencies considered by us ($\hbar\omega \approx 200$ meV) (refs. [29,32,39]).

To obtain a deeper insight into the nature of the collective excitations, we probe their frequency dependence by repeating the near-field measurements at different excitation energies, changing $\lambda_0 = 2\pi c/\omega$, where c is the speed of light. Figure 2a–e shows a dramatic change in the interference pattern for small variations in λ_0, while the boundaries of the areas where the sample is optically active

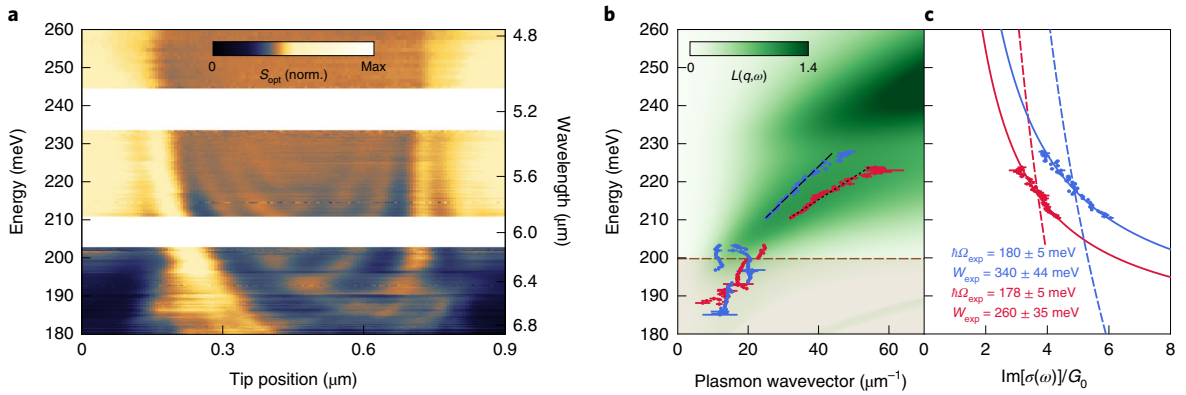

Fig. 3 | Extracting the optical conductivity from the plasmon dispersion. a, Near-field amplitude (along the dashed red arrow in Fig. 2d) for a range of excitation energies. To highlight the plasmonic modes, we normalize each line to the average near-field amplitude within the reflecting interfaces. The white gaps are gaps in the spectrum of the excitation laser. **b**, Dispersion relation $q_1(\omega)$ determined from fitting individual line traces in **a** to a sinusoidal function (red points). The blue points are obtained in a similar way but from a slightly different location (solid blue arrow in Fig. 2d). We extract the plasmon group velocity (black dashed/dotted lines) from a linear fit on the blue data points. The horizontal dashed line marks the threshold of the Reststrahlen band of hBN. The colour plot represents the loss function, calculated from the chirally symmetric continuum model[20]. **c**, Extracted values of the optical conductivity with the same colour coding as in **b**. Dots represent experimental data, dashed lines are Drude fits, while solid lines are fits with resonant profiles.

remain at a fixed position. These data show the dispersive character of the propagating collective excitations that move in Fabry–Pérot-like cavities, due to reflecting interfaces[46,47]. At the same time, the scan shown in Fig. 2f for $\hbar\omega = 170$ meV is free of any features. As $\hbar\omega$ coincides with the lower edge of the Reststrahlen band of hBN, the near-field signal is dominated by the top hBN layer. Thus, we conclude that the observed features in Fig. 2a–e originate from the TBG itself. If any contamination was present on top of the sample, or if the hBN would exhibit thickness variations, the 170 meV scan would not show such a uniform response as observed.

More quantitatively, we extract one-dimensional cuts of the measured S_{opt} along two specific lines (arrows in Fig. 2d). The resulting one-dimensional profiles are shown in Fig. 2g as lines for a few representative photon energies, while a colour map as a function of the tip position and frequency is reported in Fig. 3a (Supplementary Note 5 provides data for other line traces taken in the near-field image). The oscillating signal is well fitted by the following expression, representing a tip-launched, tip-detected wave reflected at an interface: $S_{opt}(x) = \mathrm{Re}[Ax^{-1/2}e^{2iqx}] + Bx$. Here x is the tip position along the line cut, as measured from the interface; A and q are complex fit parameters; and B represents a linear background[32]. Note the factor of two in the exponential function that appears because the collective excitation makes a full round trip between the tip and reflecting interface. Our fitting procedure yields quantitative results for the real part q_1 of the plasmon wavevector q, while the imaginary part q_2 is substantially smaller (Supplementary Note 5 provides further details).

From the extracted values of $q_1(\omega)$, we can construct a dispersion curve for the collective excitation, as shown in Fig. 3b. For energies above 200 meV, the dispersion is approximately linear with a group velocity $s \approx 0.9-1.3\times10^6\,\mathrm{m\,s^{-1}}$ (dashed and dotted lines in Fig. 3b), and crosses the $q_1 = 0$ point for $\hbar\Omega_{exp} \approx 190$ meV. For lower energies, the typical discretization pattern of a finite-size cavity appears (that is, where the distance between the reflecting interfaces is comparable to the plasmon wavelength $2\pi/q_1$). Remarkably, the group velocity is larger than theoretically anticipated. For example, in ref. [37], flat plasmonic bands were predicted, as discussed below. As we will see, this points to a larger spectral weight in the optical transitions. Clearly, the observed nearly linear dispersion, initiating from a finite energy $\hbar\Omega_{exp}$ for $q_1 = 0$, is very different from the typical Dirac plasmon dispersion of doped single-layer and bilayer graphene (Supplementary Note 6 provides more detailed comparisons). Instead, the observed linear dispersion further resembles the one of a bulk magnetoplasmon[42]: $\omega(q) = \Omega_{exp} + sq_1$.

Finally, we measured the carrier-density dependence of the dispersion of the collective excitation on one of our devices by applying a voltage bias between the TBG and metallic gate (Supplementary Note 7 provides the measurement details and experimental results). The experimental data show no noticeable change in the collective excitation wavelength inside the range of electronic densities considered. This strengthens the interpretation in terms of collective modes originating from an interband transition, as those are much less affected by the carrier density than intraband plasmons (Supplementary Note 6).

Extraction of optical conductivity

To relate our observations to electronic bands in the moiré superlattice, we extract the value of optical conductivity $\sigma(\omega)$ for the optically active regions. In the local approximation[48] (that is, where the optical conductivity is taken to be independent of q and contributions from reciprocal lattice vectors $G \neq 0$ are neglected), the longitudinal dielectric function[49] is given by $\epsilon(q,\omega) = 1 + iq^2V_{q,\omega}\sigma(\omega)/\omega$, where $V_{q,\omega} = 2\pi F(q,\omega)/[\tilde{\epsilon}(\omega)q]$ is the 2D Fourier transform of the Coulomb potential[50], the permittivity $\tilde{\epsilon}(\omega) = \sqrt{\epsilon_{\parallel}(\omega)\,\epsilon_{\perp}(\omega)}$ takes care of the optical response at frequency ω of the hBN crystal slabs[51] surrounding the TBG sample, and $F(q,\omega)$ is a form factor that takes into account the finite thickness of the hBN slabs (Supplementary Note 8). Finite-thickness effects are important close to the upper edge of the Reststrahlen band of hBN, where the in-plane permittivity $\epsilon_{\parallel}(\omega)$ vanishes and the out-of-plane decay length of the mode diverges. Neglecting the finite thickness of hBN leads to a wrong dispersion relation, yielding a collective mode that does not enter the upper Reststrahlen band (Fig. 3b). Collective modes can be found by solving $\epsilon(q,\omega) = 0$ (ref. [49]), or by looking at the peaks of the loss function $L(q,\omega) = -\mathrm{Im}(\epsilon(q,\omega)^{-1})$. From the measured collective excitation dispersion, we can find the imaginary part $\sigma_2(\omega)$ of the local conductivity, using the expression $\sigma(\omega) = i\omega/(q^2V_{q,\omega})$ and neglecting the imaginary part of q (Supplementary Note 8 shows that we can safely do this without changing the results). The results are shown in Fig. 3c.

The simplest possible fitting function of the Drude form $\sigma_2(\omega) = G_0W_0/(\hbar\omega)$, where $G_0 = 2e^2/h$ is the conductance quantum in

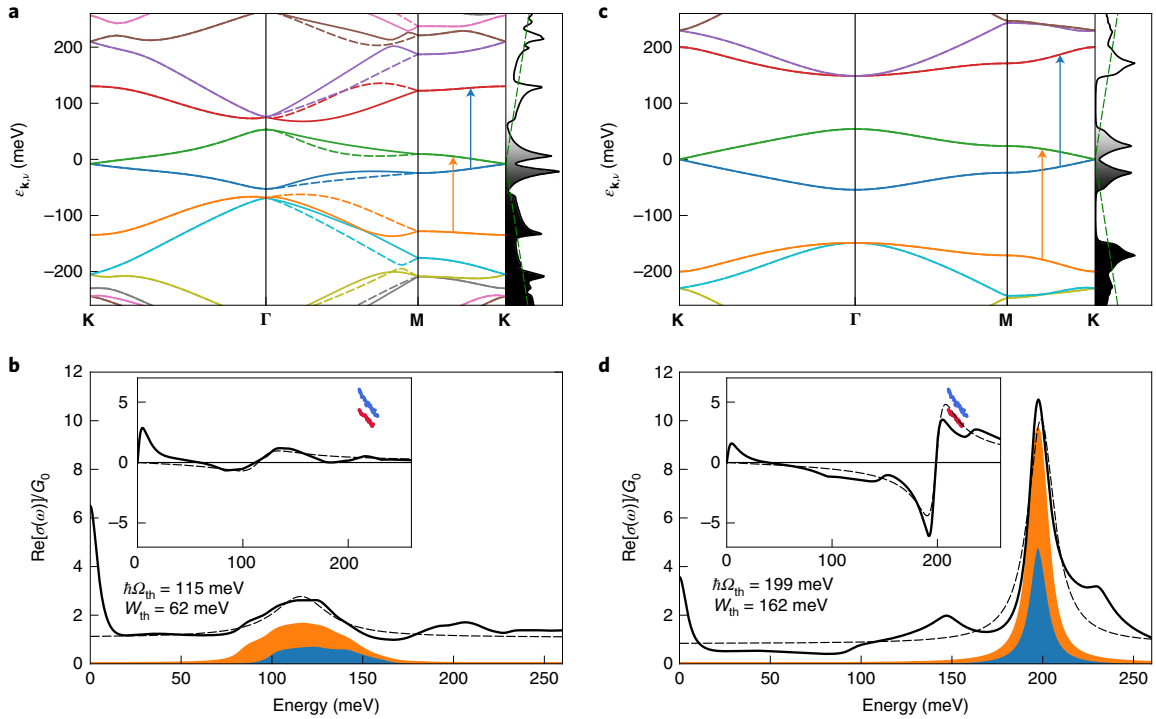

Fig. 4 | Electronic band structure and optical conductivity of TBG for $\theta = 1.35°$. a, Electronic band structure $\varepsilon_{\mathbf{k},\nu}$ of TBG with $\theta = 1.35°$ along the **KΓMK** contour of the superlattice Brillouin zone from ab initio **k·p** perturbation theory[52]. The most relevant bands are $\nu = -2$ (orange), $\nu = -1$ (blue), $\nu = 1$ (green) and $\nu = 2$ (red). The corresponding wavefunctions at the **K** point for $\nu = -1$ and $\nu = 2$ are shown in Fig. 1d. The solid (dashed) lines represent the bands in the valley close to the **K** (**K**′) point of the original graphene layers. The panel on the right shows the density of states with the colour shading representing the band occupation at room temperature, where the green dashed line represents the density of states of single-layer graphene. The vertical arrows highlight the most relevant interband optical transitions. **b**, Calculated real part of the optical conductivity (black thick line) using the Kubo formula and the band structure in **a**. Orange (blue) shading represents the contribution to the total optical conductivity of the pair of bands with $\nu = -2$, $\nu' = 1$ ($\nu = -1$, $\nu' = 2$), corresponding to the transition marked by an orange (blue) arrow in **a**. The dashed line is the Lorentzian fit to the most relevant interband feature and is used to extract the resonance parameters. The inset shows the imaginary part of the optical conductivity (normalized to G_0), together with the experimental data from Fig. 3c. **c**,**d**, Same data as in **a** and **b** but with the band structure of the chirally symmetric continuum model[20].

terms of the elementary charge e and Planck's constant h, and W_0 is a fitting parameter with dimensions of energy, yields $W_0 \approx 1{,}100$ meV (that would correspond—for two uncoupled single-layer graphene sheets—to Fermi energy $\varepsilon_F \approx 550$ meV in each layer) and a very poor fit. This confirms that our data are not consistent with a regular intraband graphene Dirac plasmon. A much better fit is obtained by using the following resonant form: $\sigma_2(\omega) = G_0 W_{\rm exp} \hbar\omega / (\hbar^2\omega^2 - \hbar^2\Omega_{\rm exp}^2)$, where $W_{\rm exp}$ and $\Omega_{\rm exp}$ are fitting parameters. We find $\hbar\Omega_{\rm exp} \approx 180$ meV and a spectral weight $W_{\rm exp} \approx 300$ meV for both presented datasets. Supplementary Note 9 further discusses the influence of a Drude response in this analysis.

Theory of interband transitions in TBG

We now seek a theoretical justification for the resonant lineshape extracted from the experimental data and for the values we have found for $\Omega_{\rm exp}$ and $W_{\rm exp}$. At the level of random phase approximation for the dynamical dielectric function[49], the unknown quantity $\sigma(\omega)$ is approximated by using its value for the non-interacting 2D electron system in TBG. The latter can be exactly calculated by employing the Kubo formula[49], once the eigenstates $|\mathbf{k},\nu\rangle$ and bands $\varepsilon_{\mathbf{k},\nu}$ of the single-particle problem are given. Here $\mathbf{k}$ represents the electronic wavevector. The quantities $|\mathbf{k},\nu\rangle$ and $\varepsilon_{\mathbf{k},\nu}$ can be found from a band structure calculation for TBG at a given θ. Here we have used the results obtained from ab initio **k·p** perturbation theory[52], which accurately accounts for the effects of intrinsic atomic relaxation in pristine samples. The resulting bands $\varepsilon_{\mathbf{k},\nu}$ are shown in Fig. 4a. We clearly see that band nesting occurs near the **K** point of the superlattice Brillouin zone, where two (relatively flat) bands—say ν and ν', connected by vertical lines with arrows in Fig. 4a—are such that $\nabla_{\mathbf{k}}\epsilon_{\mathbf{k},\nu} \simeq \nabla_{\mathbf{k}}\epsilon_{\mathbf{k},\nu'}$ in a range of values of $\mathbf{k}$. In other words, the bands are parallel to each other for a wide range of $\mathbf{k}$. The joint density of states for these pairs of bands is large at the transition frequency and the resultant optical absorption spectrum $\sigma_1(\omega) \equiv {\rm Re}[\sigma(\omega)]$ has a peak at a nearby frequency $\Omega_{\rm th}$, as shown in Fig. 4b. At the charge neutrality point, $\theta = 1.35°$ and $T = 300$ K (used for all calculations in this work), we find $\hbar\Omega_{\rm th} \approx 115$ meV and an associated spectral weight $W_{\rm th} \equiv 2\hbar\int_{\rm peak} {\rm d}\omega\sigma_1(\omega)/(\pi G_0) \approx 62$ meV. Because of causality, $\sigma_1(\omega)$ and $\sigma_2(\omega)$ are related by a Kramers–Kronig transform[49]. The resonant lineshape introduced above for $\sigma_2(\omega)$ yields $\sigma_1(\omega) = \pi G_0 W_{\rm exp}[\delta(\hbar\omega - \hbar\Omega_{\rm exp}) + \delta(\hbar\omega + \hbar\Omega_{\rm exp})]/2$. This implies that our simple resonant fitting formula for $\sigma_2(\omega)$ represents the peak seen in the microscopically calculated $\sigma_1(\omega)$ at $\Omega_{\rm th}$ (Fig. 4b) with a delta peak at $\Omega_{\rm exp}$ with spectral weight $W_{\rm exp}$.

While $\Omega_{\rm th}$ is in a reasonable agreement with $\Omega_{\rm exp}$, there is considerable disagreement between the spectral weight since $W_{\rm th} \ll W_{\rm exp}$. The sources of this spectral weight mismatch can be multiple. To gain an understanding, we resort to a more flexible continuum band structure model[53]. This contains two parameters, namely, u_0 and u_1, denoting the interlayer coupling in the AA regions and AB and BA regions, respectively. Results based on such a continuum model with the choice $u_0 = 79.7$ meV and $u_1 = 97.5$ meV (ref. [53]) present only minor quantitative differences with respect to those of the ab initio **k·p** perturbation theory (Fig. 4b and Supplementary Note 10). Also, calculations in ref. [37] give qualitatively similar

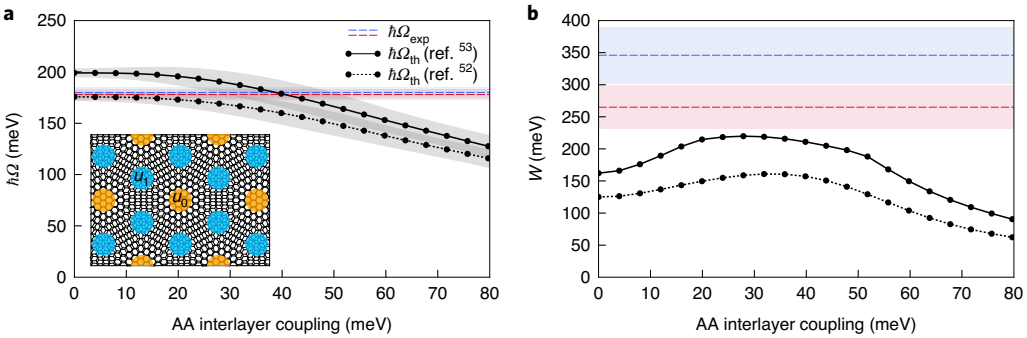

Fig. 5 | Calculated properties of the relevant interband transition as functions of tunnelling amplitude in the AA regions. a, Interband energy extracted from a Lorentzian fit of the optical conductivity. The grey shaded areas represent plus/minus half-width at half-maximum of the Lorentzian fit. In both theoretical models used in this work (refs. [52,53]), Ω_{th} decreases monotonically on increasing the AA interlayer coupling u_0. These calculations were performed by setting $\theta = 1.35°$ and $u_1 = 97.5$ meV. The blue and red dashed lines correspond to the experimentally determined resonant frequencies (Fig. 3c), with the corresponding shaded area indicating the uncertainty. The inset illustrates a triangular moiré lattice with the interlayer coupling strengths u_0 and u_1 on the AA (yellow) and AB/BA sites (blue), respectively. **b**, Same data as in **a** but for the spectral weight W_{th}. The latter displays a maximum for intermediate values of u_0.

results. The same continuum model with $u_0 = 0$ and $u_1 \neq 0$, which is endowed with unitary particle–hole symmetry, has been introduced in ref. [20] as an idealization of reality.

Intriguingly, we find that the conductivity calculated from this chirally symmetric continuum model (CS-CM) (ref. [20]), for $u_0 = 0$ and $u_1 = 97.5$ meV, displays a much better agreement with our experimental data. The bands $\varepsilon_{\mathbf{k},\nu}$ of the CS-CM are shown in Fig. 4c, while the optical absorption spectrum is reported in Fig. 4d. Also here, σ_2 displays a resonant profile, but the resonant energy is $\hbar\Omega_{th} \approx 199$ meV and the spectral weight is $W_{th} \approx 162$ meV, in much better agreement with our experimental results. The loss function calculated from this CS-CM is shown in Fig. 3b and overlaps very well with the superimposed experimental data. This suggests that the optical spectral weight is strongly enhanced in the optically active regions, and this enhancement can be explained by an effective suppression of the AA interlayer coupling in the same regions.

Motivated by this finding, we perform a systematic scan of the AA tunnelling amplitude in a range going from $u_0 = 0$ meV—corresponding to the CS-CM—to $u_0 = 79.7$ meV, which is the value given in ref. [53]. For each value of u_0, we calculate the band structure, extract the optical conductivity and fit it with a resonant profile to extract the parameters $\hbar\Omega_{th}$ and W_{th}. The results are shown in Fig. 5. The resonant frequency increases monotonically with decreasing u_0 and crosses the experimentally measured value at $u_0 \approx 40$ meV. Instead, the spectral weight has a non-monotonic behaviour but gets closest to the experimental data approximately in the range of $20 < u_0 < 40$ meV. We performed the same procedure on the ab initio $\mathbf{k}\cdot\mathbf{p}$ perturbation theory model by scaling the parameters corresponding to AA tunnelling. The results are qualitatively similar, apart from a rigid shift, as shown in Fig. 5. The rigid shift is primarily caused by a small difference between the effective AB coupling u_1 of the models. This can also be viewed as a tunable parameter of the theory and controls the location of the magic angle. An extensive theoretical discussion of the collective modes in TBG as a function of the band structure parameters can be found in ref. [38].

Therefore, our experiments suggest that, in particular regions of the sample, the AA tunnelling amplitude is substantially reduced with respect to the AB tunnelling amplitude but still has a non-vanishing value. This finding is compatible with the results of refs. [9,10,43] that reported on the gap size between the flat bands and the first excited band at the Γ point of the superlattice Brillouin zone. This quantity provides a direct measure of the difference $u_1 - u_0$ and was found to be in the range of 30–60 meV. The apparent suppression of tunnelling in the AA regions compared with the one in the AB and BA regions (that is, the fact that $u_0 < u_1$) can stem from e–e interactions or extrinsic effects. It is known[6,20] that u_1 is responsible for a (non-Abelian) gauge field acting on the electron system, while u_0 induces a scalar potential. Electron–electron interactions act between density fluctuations and therefore between longitudinal current fluctuations because of the continuity equation. Screening due to e–e interactions will therefore tend to suppress the longitudinal field due to u_0, while having a smaller impact on the transverse gauge field due to u_1.

Extrinsic factors can also alter, locally, the value of u_0. We suspect that these include the way the samples are prepared, the AFM brooming procedure (Supplementary Note 4) and possibly hBN encapsulation. It frequently happens that samples prepared in different laboratories display some macroscopic differences in their physical characteristics such as the twist angle[22], electrical transport[9–12,14,21] and spectroscopic features[16–19].

Before concluding, one may also hypothesize that our samples present a highly inhomogeneous strain distribution with patches where the associated pseudo-magnetic field B_S, pointing in the out-of-plane direction, is finite and nearly uniform[54] and regions where $B_S = 0$. A resonant conductivity profile, as observed in experiments, would naturally arise in this case at the frequency of the pseudo-cyclotron resonance. We analyse this potential explanation of our observations in Supplementary Note 11 and conclude that it is unlikely since it would require an unreasonably large amount of strain to match the observed resonant frequency.

Outlook

In summary, we have observed propagating interband collective excitations in TBG in the mid-infrared spectral region, with larger-than-expected group velocity and thus a larger spectral weight of the infrared optical transitions. The usefulness of models with reduced AA tunnel coupling[20,52,53] in interpreting our experimental data could point to the enhanced role of e–e interactions. We expect that our work will encourage further theoretical and experimental studies to assess the intrinsic (that is, e–e interactions) and extrinsic factors that can effectively renormalize the band structure parameters and the reasons for the observed sample inhomogeneity. Future low-temperature studies can moreover elucidate the role of electronic correlations in the upper bands and the contribution of collective excitations to many-body ground states[55], while terahertz near-field imaging can offer a local probe of the electronic phase transitions[56]. Finally, propagating plasmons with strong wavelength suppression, and without the need for additional doping, are of high

use for strong light–matter interactions[57], quantum plasmonics[58] or the creation of metamaterials and nano-photonic devices.

Online content

Any methods, additional references, Nature Research reporting summaries, source data, extended data, supplementary information, acknowledgements, peer review information; details of author contributions and competing interests; and statements of data and code availability are available at https://doi.org/10.1038/s41567-021-01327-8.

Received: 6 August 2020; Accepted: 14 July 2021;
Published online: 27 September 2021

References

1. Lopes Dos Santos, J. M. B., Peres, N. M. R. & Castro Neto, A. H. Graphene bilayer with a twist: electronic structure. *Phys. Rev. Lett.* **99**, 256802 (2007).
2. Suárez Morell, E., Correa, J. D., Vargas, P., Pacheco, M. & Barticevic, Z. Flat bands in slightly twisted bilayer graphene: tight-binding calculations. *Phys. Rev. B* **82**, 121407 (2010).
3. Bistritzer, R. & MacDonald, A. H. Moire bands in twisted double-layer graphene. *Proc. Natl Acad. Sci. USA* **108**, 12233–12237 (2011).
4. Li, G. et al. Observation of Van Hove singularities in twisted graphene layers. *Nat. Phys.* **6**, 109–113 (2010).
5. Nam, N. N. T. & Koshino, M. Lattice relaxation and energy band modulation in twisted bilayer graphene. *Phys. Rev. B* **96**, 075311 (2017).
6. San-Jose, P., González, J. & Guinea, F. Non-Abelian gauge potentials in graphene bilayers. *Phys. Rev. Lett.* **108**, 216802 (2012).
7. Lopes dos Santos, J. M. B., Peres, N. M. R. & Castro Neto, A. H. Continuum model of the twisted graphene bilayer. *Phys. Rev. B* **86**, 155449 (2012).
8. Guinea, F. & Walet, N. R. Electrostatic effects, band distortions, and superconductivity in twisted graphene bilayers. *Proc. Natl Acad. Sci. USA* **115**, 13174–13179 (2018).
9. Cao, Y. et al. Correlated insulator behaviour at half-filling in magic-angle graphene superlattices. *Nature* **556**, 80–84 (2018).
10. Cao, Y. et al. Unconventional superconductivity in magic-angle graphene superlattices. *Nature* **556**, 43–50 (2018).
11. Yankowitz, M. et al. Tuning superconductivity in twisted bilayer graphene. *Science* **363**, 1059–1064 (2019).
12. Lu, X. et al. Superconductors, orbital magnets and correlated states in magic-angle bilayer graphene. *Nature* **574**, 653–657 (2019).
13. Sharpe, A. L. et al. Emergent ferromagnetism near three-quarters filling in twisted bilayer graphene. *Science* **365**, 605–608 (2019).
14. Serlin, M. et al. Intrinsic quantized anomalous Hall effect in a moiré heterostructure. *Science* **367**, 900–903 (2020).
15. Tomarken, S. L. et al. Electronic compressibility of magic-angle graphene superlattices. *Phys. Rev. Lett.* **123**, 046601 (2019).
16. Choi, Y. et al. Electronic correlations in twisted bilayer graphene near the magic angle. *Nat. Phys.* **15**, 1174–1180 (2019).
17. Kerelsky, A. et al. Maximized electron interactions at the magic angle in twisted bilayer graphene. *Nature* **572**, 95–100 (2019).
18. Xie, Y. et al. Spectroscopic signatures of many-body correlations in magic-angle twisted bilayer graphene. *Nature* **572**, 101–105 (2019).
19. Jiang, Y. et al. Charge order and broken rotational symmetry in magic-angle twisted bilayer graphene. *Nature* **573**, 91–95 (2019).
20. Tarnopolsky, G., Kruchkov, A. J. & Vishwanath, A. Origin of magic angles in twisted bilayer graphene. *Phys. Rev. Lett.* **122**, 106405 (2019).
21. Yoo, H. et al. Atomic and electronic reconstruction at the van der Waals interface in twisted bilayer graphene. *Nat. Mater.* **18**, 448–453 (2019).
22. Uri, A. et al. Mapping the twist-angle disorder and Landau levels in magic-angle graphene. *Nature* **581**, 47–52 (2020).
23. Liu, X. et al. Tunable spin-polarized correlated states in twisted double bilayer graphene. *Nature* **583**, 221–225 (2020).
24. Cao, Y. et al. Tunable correlated states and spin-polarized phases in twisted bilayer–bilayer graphene. *Nature* **583**, 215–220 (2020).
25. Shen, C. et al. Correlated states in twisted double bilayer graphene. *Nat. Phys.* **16**, 520–525 (2020).
26. Chen, G. et al. Evidence of a gate-tunable Mott insulator in a trilayer graphene moiré superlattice. *Nat. Phys.* **15**, 237–241 (2019).
27. Basov, D. N., Fogler, M. M. & Garcia de Abajo, F. J. Polaritons in van der Waals materials. *Science* **354**, aag1992 (2016).
28. Low, T. et al. Polaritons in layered two-dimensional materials. *Nat. Mater.* **16**, 182–194 (2017).
29. Sunku, S. S. et al. Photonic crystals for nano-light in moiré graphene superlattices. *Science* **362**, 1153–1156 (2018).
30. Ni, G. X. et al. Plasmons in graphene moiré superlattices. *Nat. Mater.* **14**, 1217–1222 (2015).
31. Hu, F. et al. Real-space imaging of the tailored plasmons in twisted bilayer graphene. *Phys. Rev. Lett.* **119**, 247402 (2017).
32. Woessner, A. et al. Highly confined low-loss plasmons in graphene–boron nitride heterostructures. *Nat. Mater.* **14**, 421–425 (2015).
33. Moon, P. & Koshino, M. Optical absorption in twisted bilayer graphene. *Phys. Rev. B* **87**, 205404 (2013).
34. Stauber, T., San-Jose, P. & Brey, L. Optical conductivity, Drude weight and plasmons in twisted graphene bilayers. *New J. Phys.* **15**, 113050 (2013).
35. Tabert, C. J. & Nicol, E. J. Optical conductivity of twisted bilayer graphene. *Phys. Rev. B* **87**, 121402 (2013).
36. Lewandowski, C. & Levitov, L. Intrinsically undamped plasmon modes in narrow electron bands. *Proc. Natl Acad. Sci. USA* **116**, 20869–20874 (2019).
37. Stauber, T. & Kohler, H. Quasi-flat plasmonic bands in twisted bilayer graphene. *Nano Lett.* **16**, 6844–6849 (2016).
38. Novelli, P., Torre, I., Koppens, F. H. L., Taddei, F. & Polini, M. Optical and plasmonic properties of twisted bilayer graphene: impact of interlayer tunneling asymmetry and ground-state charge inhomogeneity. *Phys. Rev. B* **102**, 125403 (2020).
39. Das Sarma, S. & Li, Q. Intrinsic plasmons in two-dimensional Dirac materials. *Phys. Rev. B* **87**, 235418 (2013).
40. Ou, J.-Y. et al. Ultraviolet and visible range plasmonics in the topological insulator $Bi_{1.5}Sb_{0.5}Te_{1.8}Se_{1.2}$. *Nat. Commun.* **5**, 5139 (2014).
41. Dubrovkin, A. M. et al. Visible range plasmonic modes on topological insulator nanostructures. *Adv. Opt. Mater.* **5**, 1600768 (2017).
42. Fetter, A. L. Edge magnetoplasmons in a two-dimensional electron fluid confined to a half-plane. *Phys. Rev. B* **33**, 3717–3723 (1986).
43. Cao, Y. et al. Superlattice-induced insulating states and valley-protected orbits in twisted bilayer graphene. *Phys. Rev. Lett.* **117**, 116804 (2016).
44. Kim, K. et al. van der Waals heterostructures with high accuracy rotational alignment. *Nano Lett.* **16**, 1989–1995 (2016).
45. Keilmann, F. & Hillenbrand, R. Near-field microscopy by elastic light scattering from a tip. *Phil. Trans. R. Soc. Lond. A* **362**, 787–805 (2004).
46. Jiang, B.-Y. et al. Plasmon reflections by topological electronic boundaries in bilayer graphene. *Nano Lett.* **17**, 7080–7085 (2017).
47. Chen, J. et al. Strong plasmon reflection at nanometer-size gaps in monolayer graphene on SiC. *Nano Lett.* **13**, 6210–6215 (2013).
48. Avouris, P., Heinz, T. F. & Low, T. *2D Materials* (Cambridge Univ. Press, 2017).
49. Giuliani, G. F. & Vignale, G. *Quantum Theory of the Electron Liquid* (Cambridge Univ. Press, 2005).
50. Alonso-González, P. et al. Acoustic terahertz graphene plasmons revealed by photocurrent nanoscopy. *Nat. Nanotechnol.* **12**, 31–35 (2017).
51. Cai, Y., Zhang, L., Zeng, Q., Cheng, L. & Xu, Y. Infrared reflectance spectrum of BN calculated from first principles. *Solid State Commun.* **141**, 262–266 (2007).
52. Carr, S., Fang, S., Zhu, Z. & Kaxiras, E. Exact continuum model for low-energy electronic states of twisted bilayer graphene. *Phys. Rev. Res.* **1**, 013001 (2019).
53. Koshino, M. et al. Maximally localized Wannier orbitals and the extended Hubbard model for twisted bilayer graphene. *Phys. Rev. X* **8**, 031087 (2018).
54. Guinea, F., Katsnelson, M. I. & Geim, A. K. Energy gaps and a zero-field quantum Hall effect in graphene by strain engineering. *Nat. Phys.* **6**, 30–33 (2009).
55. Sharma, G., Trushin, M., Sushkov, O. P., Vignale, G. & Adam, S. Superconductivity from collective excitations in magic-angle twisted bilayer graphene. *Phys. Rev. Res.* **2**, 022040 (2020).
56. Calderón, M. J. & Bascones, E. Correlated states in magic angle twisted bilayer graphene under the optical conductivity scrutiny. *npj Quantum Mater.* **5**, 57 (2020).
57. Rivera, N. & Kaminer, I. Light–matter interactions with photonic quasiparticles. *Nat. Rev. Phys.* **2**, 538–561 (2020).
58. Fitzgerald, J. M., Narang, P., Craster, R. V., Maier, S. A. & Giannini, V. Quantum plasmonics. *Proc. IEEE* **104**, 2307–2322 (2016).

Data availability

Source data are provided with this paper. All other data that support the plots within this paper and other findings of this study are available from the corresponding authors upon reasonable request.

Acknowledgements

We thank F. Vialla for providing the illustration in Fig. 1a. We acknowledge A. H. MacDonald, F. Guinea, T. Stauber, F. Mauri, R. K. Kumar and A. Tomadin for useful discussions. F.H.L.K. acknowledges support from the ERC TOPONANOP (grant agreement no. 726001), the government of Spain (PID2019-106875GB-I00; Severo Ochoa CEX2019-000910-S), Fundació Cellex, Fundació Mir-Puig, and Generalitat de Catalunya (CERCA, AGAUR, SGR 1656). Furthermore, the research leading to these results has received funding from the European Union's Horizon 2020 under grant agreement no. 881603 (Graphene flagship Core3). N.C.H.H., I.T., P.S., D.B.-R., H.H.S., D.K.E. and F.H.L.K. acknowledge financial support from the Spanish Ministry of Economy and Competitiveness through the 'Severo Ochoa' program for Centres of Excellence in R&D (SEV-2015-0522), from Fundació Privada Cellex and Fundació Privada Mir-Puig, and from Generalitat de Catalunya through the CERCA program. N.C.H.H. acknowledges funding from the European Union's Horizon 2020 research and innovation programme under the Marie Skłodowska-Curie grant agreement no. 665884. I.T. acknowledges funding from the Spanish Ministry of Science, Innovation and Universities (MCIU) and State Research Agency (AEI) via the Juan de la Cierva fellowship no. FJC2018-037098-I. D.B.-R. acknowledges funding from the 'Secretaria d'Universitats i Recerca de la Generalitat de Catalunya i del Fons Social Europeu'. H.H.S. acknowledges funding under the Marie Skłodowska-Curie grant agreement no. 843830. D.K.E. acknowledges support from the Horizon 2020 programme under grant agreement no. 820378, Project 2D·SIPC and the La Caixa Foundation. P.N. and M.P. have been supported by the European Union's Horizon 2020 research and innovation programme under grant agreement no. 785219, GrapheneCore2. Work at MIT has been primarily supported by the National Science Foundation (award DMR-1809802), the Center for Integrated Quantum Materials under NSF grant DMR-1231319, and the Gordon and Betty Moore Foundation's EPiQS Initiative through grant GBMF9643 to P.J.-H. for device fabrication, transport measurements and data analysis. This work was performed in part at the Harvard University Center for Nanoscale Systems (CNS), a member of the National Nanotechnology Coordinated Infrastructure Network (NNCI), which is supported by the National Science Foundation under NSF ECCS award no. 1541959. D.R.-L. acknowledges partial support from Fundacio Bancaria 'la Caixa' (LCF/BQ/AN15/10380011). S.F. was supported by the STC Center for Integrated Quantum Materials, NSF grant no. DMR-1231319. S.C. and E.K. were supported by ARO MURI Award W911NF-14-0247. K.W. and T.T. acknowledge support from the Elemental Strategy Initiative conducted by the MEXT, Japan, and the CREST (JPMJCR15F3), JST.

Author contributions

F.H.L.K. and P.J.-H. designed the experiment. N.C.H.H. performed the near-field measurements with assistance from D.B.-R. and H.H.S. D.R.-L., Y.C. and P.S. fabricated the devices and performed transport measurements under the supervision of P.J.-H. and D.K.E. N.C.H.H. and I.T. performed the data analysis. I.T. and P.N. developed the theory part with inputs from M.P. and F.H.L.K. S.C. and S.F. provided the band structures based on ab initio **k·p** perturbation theory under the supervision of E.K. K.W. and T.T. provided the hBN crystals. F.H.L.K., M.P. and P.J.-H. supervised the project. I.T., N.C.H.H., M.P. and F.H.L.K. wrote the manuscript with input from all the authors.

Competing interests

The authors declare no competing interests.

Additional information

Supplementary information The online version contains supplementary material available at https://doi.org/10.1038/s41567-021-01327-8.

Correspondence and requests for materials should be addressed to Pablo Jarillo-Herrero, Marco Polini or Frank H. L. Koppens.

Peer review information *Nature Physics* thanks the anonymous reviewers for their contribution to the peer review of this work.